Available on the CERN CDS information server **CMS PAS HIN-19-013**

# CMS Physics Analysis Summary

Contact: cms-pag-conveners-heavyions@cern.ch 2020/07/30

# Study of in-medium modification of dijets in PbPb collisions at 5.02 TeV

The CMS Collaboration

## Abstract

Modifications to the distribution of charged particles with respect to high transverse momentum ($p_{\mathrm{T}}$) jets passing through a quark-gluon plasma are explored. Jets corresponding to dijet selection where the leading and subleading jets are back-to-back are studied in lead-lead (PbPb) and proton-proton (pp) collisions. Correlations of charged particles are measured in relative pseudorapidity and relative azimuth from the jet axes. Jet momentum density profiles ("jet shapes") are determined. The events are categorized in bins of collision centrality, charged particle $p_{\mathrm{T}}$ and dijet momentum balance $x_j$, which is the ratio between the subleading and leading jet $p_{\mathrm{T}}$. In comparing the PbPb and pp collision results, modifications to the charged particle yields is found to depend on the $x_j$ value. Modifications to both the charged-particle pseudorapidity dependence and the jet momentum density profile are observed to be greater for the leading jet in more momentum balanced conditions. The modifications become more pronounced with respect to the subleading jet for events with a larger dijet momentum imbalance.

# 1 Introduction

High transverse momentum ($p_{\mathrm{T}}$) jets are associated with partons produced in the initial hard scatterings of heavy ion collisions and may be used to probe the properties of the quark gluon plasma (QGP) as they pass through this medium. One example of such a response is jet quenching [1], which was first observed at the BNL RHIC [2, 3] and subsequently at the CERN LHC [4–7]. Jet quenching is seen as a suppression of high-$p_{\mathrm{T}}$ leading charged particle and jet yields in head-on PbPb collisions relative to pp reference data. Using data collected at the LHC, studies have shown that the jet structure is also modified by the medium, as observed with precise measurements of the fragmentation pattern [8, 9] and the distribution of charged-particle $p_{\mathrm{T}}$ as a function of radial distance from the jet axis [10]. These modifications are found to extend to large distances in relative pseudorapidity ($\Delta\eta$) and relative azimuth ($\Delta\phi$) with respect to the jet axis [11–14]. Various theoretical models have attempted to account for these modifications [15–20] and while most models reproduce the modifications close to the jet axis, the large modifications observed far from the jet axis $\Delta r > 0.5$ are not yet well understood.

This analysis uses LHC data collected by the CMS experiment at a collision energy of $\sqrt{s_{\mathrm{NN}}} = 5.02$ TeV in 2017 and 2018, corresponding to integrated luminosities of 320 $\mathrm{pb}^{-1}$ for pp and 1.7 $\mathrm{nb}^{-1}$ for PbPb collisions, respectively. Events are selected with nearly back-to-back, high-$p_{\mathrm{T}}$ leading and subleading jet pairs. Correlations in relative pseudorapidity ($\Delta\eta$) are measured between both the leading and subleading jet axes and charged-particle tracks, requiring relative azimuth $|\Delta\varphi| < 1.0$. The "jet shape," which is the distribution of charged-particle transverse momentum ($p_{\mathrm{T}}^{\mathrm{trk}}$) with the respect to the jet axis, is also studied. Results are presented differentially as a function of PbPb collision centrality (i.e. the degree of overlap of the colliding nuclei, with head-on collisions defined as "most central"), $p_{\mathrm{T}}^{\mathrm{trk}}$, and dijet momentum balance $x_j = p_{\mathrm{T}}^{\mathrm{subleading}}/p_{\mathrm{T}}^{\mathrm{leading}}$.

# 2 The CMS experiment

The central feature of the CMS apparatus is a superconducting solenoid of 6 m internal diameter, providing a magnetic field of 3.8 T. Within the solenoid volume are a silicon pixel and strip tracker, a lead tungstate crystal electromagnetic calorimeter (ECAL), and a brass and scintillator hadron calorimeter (HCAL), with both ECAL and HCAL composed of barrel and endcap sections. Two hadronic forward (HF) steel and quartz-fiber calorimeters complement the barrel and endcap detectors, extending the calorimeter from the range $|\eta| < 3.0$ provided by the barrel and endcap out to $|\eta| < 5.2$. The HF calorimeters are segmented to form $0.175 \times 0.175$ ($\Delta\eta \times \Delta\phi$) towers. The sum of the transverse energies detected in the HF detectors ($3.0 < |\eta| < 5.2$) is used to define the event centrality in PbPb events and to divide the event sample into centrality classes, each representing a percentage of the total nucleus-nucleus hadronic interaction cross section. A detailed description of the centrality determination can be found in Ref. [21].

Jets used in this analysis are reconstructed within the range $|\eta| < 1.6$. In the region $|\eta| < 1.74$ the HCAL cells have widths of 0.087 in both $\eta$ and $\varphi$ and thus provide high granularity. Within the central barrel region of $|\eta| < 1.48$, the HCAL cells map onto $5 \times 5$ ECAL crystal arrays to form calorimeter towers projecting radially outwards from the nominal interaction point. Within each tower, the energy deposits in ECAL and HCAL cells are summed to define the calorimeter tower energies.

The CMS silicon tracker measures charged-particle tracks within $|\eta| < 2.5$. It consists of 1440 silicon pixel and 15 148 silicon strip detector modules. For charged particles with $1 < p_{\mathrm{T}} <$

10 GeV in the barrel region, the track resolutions are typically 1.5% in $p_T$ and 25-90 (45-150) $\mu$m in the impact parameter direction transverse (longitudinal) to the colliding beams [22]. A detailed description of the CMS detector, together with a definition of the coordinate system used and the relevant kinematic variables, can be found in Ref. [23].

## 3 Event selection

The pp and PbPb data are selected with a calorimeter-based trigger that uses the anti-$k_T$ jet clustering algorithm with distance parameter of $R = 0.4$ [24]. The trigger requires events to contain at least one jet with $p_T > 80$ and 100 GeV for pp and PbPb collisions, respectively. For PbPb collisions, the underlying event background is subtracted from the jet $p_T$ using an iterative method [25] before comparing to the threshold. The data selected by this trigger is referred to as "jet-triggered". For the PbPb event selection, a minimum bias triggered [26] sample is also used in the analysis.

To reduce contamination from non-collision events, including calorimeter noise and beam-gas collisions, vertex and noise filters are applied offline to both the pp and PbPb data as described for previous analyses of lower energy data [5, 6]. These filters include requirements that each of at least three HF towers on either side of the interaction point have tower energy above 3 GeV and that the vertex position along the beam line lies within 15 cm of the nominal interaction point.

Monte Carlo (MC) simulated event samples are used to evaluate the performance of the event reconstruction, particularly the track reconstruction efficiency and the jet energy response and resolution. The hard scattering, parton shower and fragmentation of the partons are modeled using the PYTHIA 8 event generator with tune CP5 [27, 28]. The specific PYTHIA version used is 8.226 and the PDF set is NNPDF3.1 at NNLO [29]. The CMS detector response is simulated using the GEANT4 toolkit [30]. The soft underlying event for the PbPb collisions is simulated by the HYDJET event generator [31]. The energy density in the HYDJET simulation is tuned to match the data by shifting the centrality definition in plain HYDJET by 5%. This tuning gives the best match in random cone energy densities between data and HYDJET. To simulate full PbPb collision jet events, PYTHIA 8 generated hard events are embedded into soft HYDJET events. This sample is denoted as PYTHIA+HYDJET.

In PbPb collisions, jets are produced more frequently in central events than in non-central events because of the large number of binary collisions per nuclear interaction. A centrality-based reweighting is applied to the PYTHIA+HYDJET sample in order to match the centrality distribution of the jet-triggered PbPb data. An additional reweighting procedure is performed to match the simulated vertex distributions to data for both the pp and PbPb samples.

Each event is required to have a dijet containing a leading jet with $p_T > 120$ GeV and a subleading jet with $p_T > 50$ GeV. These jets are further required to be within $|\eta| < 1.6$ and almost back-to-back in $\varphi$ by imposing a condition $\Delta\varphi > 5\pi/6$. These events containing pairs of back-to-back leading and subleading jets are referred as dijet events for the remainder of the note. The dijets selected for the analysis must consist of the highest and the second highest $p_T$ jets reconstructed in each event. For the reminder of the note, the term dijet refers to this leading dijet in each event.

# 4 Jet and track reconstruction

For this analysis, jets in both pp and PbPb collisions are reconstructed using the anti-$k_T$ algorithm with a radius parameter $R = 0.4$, as implemented in the FastJet framework [32]. A particle flow algorithm using an optimized combination of information from various elements of the CMS detector is used to reconstruct leptons, photons and charged and neutral hadrons [33]. These particle flow candidates are used to reconstruct the jets studied in this analysis. The jets are first clustered using E-scheme clustering [32], and for these jets the jet axis is recalculated with the winner-take-all algorithm [34, 35] using the same constituents. In the E-scheme clustering, particle pairs are combined to form pseudo-jets (an object that is a combination of particles or other pseudo-jets), with the direction of the new pseudo-jet given by the sum of the four-momenta of the particles. In the winner-take-all scheme the direction of the new pseudo-jet follows the direction of the particle with higher $p_T$. It follows that the E-scheme axis is given by the sum of pseudo-jet four-momenta, while the winner-take-all axis follows the axis of the hardest pseudo-jet. The winner-take-all axis is preferred in this analysis over the default E-scheme axis because of an artificial structure, seen as a strong depletion of particles just outside of the jet cone radius, created by the E-scheme axis.

In order to subtract the soft underlying event (UE) contribution to the jet energy in PbPb collisions on an event-by-event basis, an iterative algorithm [36] is employed. The mean value, $\langle E_{PF} \rangle$, and dispersion, $\sigma(E_{PF})$, of the energies from the particle flow candidates are calculated in $\eta$ strips [5, 6]. Then, the azimuthal modulation of the background activity is determined with respect to event plane angles for the second and third order harmonics of the global charged particle densities found using the HF calorimeters [37]. Fits are then performed on the azimuthal angle distribution of charged hadron particle flow candidates with $0.3 < p_T < 3.0$ GeV and $|\eta| < 1$ to estimate the UE energy variations due to elliptic and triangular flow. A constituent subtraction method [38] is used to subtract the contribution due to azimuthal anisotropies. This involves a particle-by-particle approach that corrects jet constituents based on the local average underlying event density, which is determined using the fit method described above and varying as a function of the azimuthal angle in fine bins of $\eta$. In pp collisions, where the UE level is negligible, jets are reconstructed without UE subtraction.

The track reconstruction used in pp and PbPb collisions is described in Ref. [39]. It is required that the relative $p_T$ uncertainty of tracks is less than 10% in both pp and PbPb collisions. In PbPb collisions, tracks must also have at least 11 hits in the tracker layers and satisfy a stringent fit quality requirement, specifically that the $\chi^2$, divided by both the number of degrees of freedom and the number of tracker layers hit, be less than 0.18. To decrease the likelihood of counting nonprimary charged particles originating from secondary decay products, a selection requirement of less than 3 standard deviations is applied on the significance of the distance of closest approach to at least one primary vertex in the event, for both collision systems. Finally, for PbPb collisions a selection based on the relationship of a track to calorimeter energy deposits along its trajectory is applied in order to curtail the contribution of misreconstructed tracks with very high $p_T$. Tracks with $p_T > 20$ GeV are required to have an associated energy deposit of at least half their momentum in the CMS calorimeters. Corrections for tracking efficiency, detector acceptance, and misreconstruction rate are obtained following the procedure in Ref. [40].

Table 1: Number of events for pp and for different PbPb centrality bins within stated $x_j$ ranges. The numbers in parentheses show the fraction of events in each $x_j$ bin for a given centrality.

| $x_j$ | $0-10\%$ | $10-30\%$ | $30-50\%$ | $50-90\%$ | pp |
|---|---|---|---|---|---|
| $0 < x_j < 0.6$ | $2.3 \cdot 10^5(40\%)$ | $2.3 \cdot 10^5(35\%)$ | $0.76 \cdot 10^5(29\%)$ | $0.20 \cdot 10^5(26\%)$ | $31 \cdot 10^5(24\%)$ |
| $0.6 < x_j < 0.8$ | $1.9 \cdot 10^5(33\%)$ | $2.3 \cdot 10^5(34\%)$ | $0.92 \cdot 10^5(36\%)$ | $0.27 \cdot 10^5(35\%)$ | $46 \cdot 10^5(36\%)$ |
| $0.8 < x_j < 1$ | $1.6 \cdot 10^5(27\%)$ | $2.0 \cdot 10^5(31\%)$ | $0.92 \cdot 10^5(35\%)$ | $0.31 \cdot 10^5(39\%)$ | $51 \cdot 10^5(40\%)$ |
| $x_j > 0$ | $5.8 \cdot 10^5$ | $6.6 \cdot 10^5$ | $2.6 \cdot 10^5$ | $0.78 \cdot 10^5$ | $130 \cdot 10^5$ |

## 5 Jet-charged particle angular correlations

Correlations between reconstructed jets and charged-particle tracks are studied by forming a two-dimensional histogram of the $\Delta\eta$ and $\Delta\varphi$ values of the charged particles relative to the jet axis. Events in PbPb collisions are divided into four centrality intervals, 0-10%, 10-30%, 30-50% and 50-90%, based on the total energy collected in the HF calorimeter. The events are also binned by charged particle $p_{\mathrm{T}}$ with bin boundaries of 0.7, 1, 2, 3, 4, 8, 12, and 300 GeV and in dijet momentum balance $x_j = p_{\mathrm{T}}^{\mathrm{subleading}}/p_{\mathrm{T}}^{\mathrm{leading}}$ with bin boundaries of 0, 0.6, 0.8, and 1. For the jet shape measurement, each charged particle is weighted by its $p_{\mathrm{T}}$ value. The two-dimensional correlation histograms are filled by correlating all the charged particles in the event with the leading jet and the subleading jet, separately. All of the two-dimensional correlation plots are normalized per dijet pair. The numbers of dijets in our data samples for each $x_j$ and centrality bin are summarized in Table 1.

The mixed event method is employed to correct for limited detector acceptance. In this method the jet and charged particles from different events are correlated to ensure that no physical correlations exist in the distribution. Because the detector has limited acceptance in pseudorapidity, it is more probable to find jet-charged particle pairs with small rather than large $\Delta\eta$ values. Thus the raw correlations have a shape where the yield strongly decreases towards large $\Delta\eta$. Mixed event distributions capture this acceptance structure. It is required that the vertex positions along the beam axis match within 0.5 cm and that the centrality match within 0.5% for the mixed events. For the pp collisions, a jet-triggered sample is used to find the mixed events, while for PbPb collisions a minimum bias sample is used to properly capture the long range correlations. This procedure is similar to that done in previous analyses [13, 14]. Denoting the number of dijets satisfying the selection criteria as $N_{\mathrm{dijet}}$, the per-jet associated yield corrected for the acceptance effects is given by

$$\frac{1}{N_{\mathrm{dijet}}}\frac{\mathrm{d}^2N}{\mathrm{d}\Delta\eta\mathrm{d}\Delta\varphi} = \frac{ME(0,0)}{ME(\Delta\eta,\Delta\varphi)}S(\Delta\eta,\Delta\varphi)\,, \tag{1}$$

where the signal pair distribution $S(\Delta\eta,\Delta\varphi)$ represents the per dijet normalized yield of jet-charged particle pairs from the same event,

$$S(\Delta\eta,\Delta\varphi) = \frac{1}{N_{\mathrm{dijet}}}\frac{\mathrm{d}^2N^{\mathrm{same}}}{\mathrm{d}\Delta\eta\mathrm{d}\Delta\varphi}\,, \tag{2}$$

and the mixed-event pair distribution $ME(\Delta\eta,\Delta\varphi)$ is given by

$$ME(\Delta\eta, \Delta\varphi) = \frac{\mathrm{d}^2 N^{\mathrm{mixed}}}{\mathrm{d}\Delta\eta \mathrm{d}\Delta\varphi} \,. \tag{3}$$

The ratio $ME(0,0)/ME(\Delta\eta, \Delta\varphi)$ is the normalized correction factor. The maximum of the mixed event distribution can be found at $(0,0)$ as no pairs with $\Delta\eta = 0$ are lost due to acceptance effects.

The acceptance corrected distribution has contributions from several different sources. The jet correlation shows up as a Gaussian like peak around $(\Delta\eta, \Delta\varphi) = (0,0)$ and a peak prolonged in $\Delta\eta$ around $\Delta\varphi = \pi$. While the jet energy and momenta are corrected for the global event geometry as previously discussed, the background particles correlated with the jet will remain in the jet-charged particle signal, and thus have to be removed. To model this background, the $\Delta\varphi$ distribution is averaged over the region $1.5 < |\Delta\eta| < 2.5$ on the "near" side ( $-\pi/2 < \Delta\varphi < \pi/2$) of the jet. The same background region criteria is used for correlations of charged particles with both leading and subleading jets and the backgrounds are combined to cover the full $\Delta\varphi$ range. This procedure is applied to avoid an "eta swing" effect. Momentum conservation dictates that the two jets must be approximately back-to-back in $\Delta\varphi$, but no such requirement exists for the $\Delta\eta$ separation. Thus, the away side ($|\Delta\varphi| > \pi/2$) jet peak in jet-charged particle correlation distributions is prolonged in $\Delta\eta$ and would still be present in the region used to estimate the background. The background determined using the respective near-side components is propagated to the full $(\Delta\eta, \Delta\varphi)$ plane and subtracted from the acceptance corrected distribution to obtain the jet signal.

Finally, simulation-based corrections are applied to account for a bias toward selecting jets with a harder constituent $p_{\mathrm{T}}$ spectrum (affecting PbPb and pp events similarly) and a bias toward selecting jets that are affected by upward fluctuations in the soft underlying event (relevant for PbPb events only). Jets with a harder constituent $p_{\mathrm{T}}$ spectrum are more likely to be successfully reconstructed than jets with a softer constituent $p_{\mathrm{T}}$ spectrum because the calorimeter response does not scale linearly with incident particle energy, resulting in a bias toward the selection of jets with fewer associated particles. A residual correction for this bias is derived following the method described in Refs. [11–13], by comparing per-jet yields of generated particles correlated to reconstructed jets relative to those correlated to generated jets. This correction is derived using a PYTHIA simulation for pp events and considering only generated particles coming from the embedded PYTHIA hard process in PYTHIA+HYDJET simulation for PbPb events.

For PbPb events, there is an additional jet reconstruction bias towards the selection of jets that are produced in the vicinity of upward fluctuations in the underlying event. Because of the steeply falling jet $p_{\mathrm{T}}$ spectrum, an excess in the background yield is expected below the jet peak as upward fluctuations of the background increase the probability of finding a jet that passes the jet selection cuts more than downwards fluctuations decrease this probability. To account for this bias, a similar procedure to that outlined in Refs. [12, 13, 41] is followed. Correlations in the PYTHIA+HYDJET sample between reconstructed jets and generated particles are compared to those from the HYDJET underlying event, excluding particles from the embedded hard process. This gives an estimate of the underlying event yield on top of which the jet correlations are sitting in the data. To reduce the fluctuations in the generated sample, the obtained distribution is symmeterized in $\Delta\eta$ and $\Delta\varphi$ before application as a correction to the PbPb data.

# 6 Systematic uncertainties

The following sources of uncertainty are considered for this analysis:

- Background fluctuation bias. Three different sources are considered for this uncertainty. The first is a difference between the quark and gluon jet fraction found in simulation and in data. The potential difference is estimated to be less than 25% using a template fit to particle flow candidate distribution in the data. Then the uncertainty is estimated by varying the quark/gluon jet fraction in the simulation by this amount. The second source considers the difference in the background energy density between simulation and data and is estimated by random cone studies. The uncertainty is determined by varying centrality definition of the HYDJET simulation by 1% point around the best match to data. Finally there is the uncertainty on the background level for the simulation from which the background correction is derived. The uncertainty is obtained in a similar manner as for data, as discussed below.
- Jet fragmentation bias. Most of the detector and resolution effects contributing to the jet fragmentation bias uncertainty come from the uncertainty in the ratios of quark and gluon jets between data and simulation, as discussed for the background fluctuation bias. Deriving the corrections separately for quark and gluon jets and varying their relative contribution, the estimated fractions translate to 10% of the total correction as a systematic uncertainty for the fragmentation bias.
- Jet energy scale. The jet energy scale uncertainties are estimated by varying the jet energy corrections within their uncertainties and seeing how these changes affect the final correlations. The jet energy uncertainty is discussed in detail in Ref. [42].
- Jet resolution. The jet resolution uncertainty is estimated by smearing the jet resolution estimated from the simulation by 20% and comparing the smeared results to the nominal ones. The 20% comes from the maximal estimated difference in jet resolution between data and simulation.
- Trigger bias. The calorimeter based trigger with the threshold of 100 GeV is not fully efficient for the PbPb collisions. To see if this has an effect on the final results, the analysis was repeated requiring a prescaled trigger with a threshold of 80 GeV and the results with this trigger were compared to the nominal ones. For the leading jet shapes it was found that there is a 2% difference in the bin closest to the jet axis, while for the other bins and for the subleading jets the difference in negligible. The 2% difference is applied as a systematic uncertainty.
- Tracking efficiency. This uncertainty is estimated from the ratio of corrected reconstructed yields and generated yields by using generator level charged particles as a "truth" reference. The systematic uncertainty from tracking efficiency closure is found to be within 3% in PbPb and 1% in pp collisions. An extra uncertainty is added to tracks close to the jet axis, as in the high multiplicity environment around the jet the tracking efficiency is found to be 1-2% worse than far away from the jets. To account for the possible track reconstruction differences in data and simulation, a residual uncertainty in track reconstruction efficiency and fake rate corrections is estimated to be 5% for PbPb and 2.4% for pp collisions.
- Pair acceptance. The uncertainty arising from pair-acceptance effects is estimated by considering the sideband asymmetry after dividing by the mixed-event background. Each sideband region of the acceptance corrected $\Delta\eta$ distribution ($-2.5 < \Delta\eta < -1.5$ and $1.5 < \Delta\eta < 2.5$) is separately fit with a horizontal line. The difference between the average yield in the positive and negative sides is assigned as a systematic uncertainty.
- Background subtraction. Uncertainties resulting from the background subtraction

are determined by considering the two parts of the sideband region, $1.5 < |\Delta\eta| < 2.0$ and $2.0 < |\Delta\eta| < 2.5$, after background subtraction. The average yield is calculated in each of the regions and the larger deviation from zero is assigned as a systematic uncertainty.

The total systematic uncertainties are obtained by adding all the individual components together in quadrature. For the leading jet correlations the uncertainties integrated in $x_j$ and $\Delta r$ are listed in Table 2 and for subleading jet correlations in Table 3.

| Source | 0–10% | 10–30% | 30–50% | 50–90% | pp |
|---|---|---|---|---|---|
| Background fluctuation bias | 0-4% | 0-3% | 0-2% | 0-1% | 0% |
| Jet fragmentation bias | 0-3% | 0-2% | 0-2% | 0-2% | 0-1% |
| Residual jet energy scale | 3-7% | 3-8% | 3-8% | 3-9% | 1-9% |
| Jet resolution | 1-3% | 1-3% | 1-3% | 1-3% | 0-2% |
| Tracking efficiency | 6-8% | 6-8% | 6-7% | 6-7% | 3% |
| Pair-acceptance corrections | 0-3% | 0-3% | 0-3% | 0-3% | 0-1% |
| Background subtraction | 0-4% | 0-3% | 0-3% | 0-3% | 0-2% |
| Total | 8-14% | 8-12% | 8-12% | 8-11% | 3-10% |

Table 2: Systematic uncertainties for the leading jet shape components, integrated in $\eta$, and $\Delta r$, and shown for pp and centrality binned PbPb collisions. The ranges correspond to the $p_{\mathrm{T}}$ dependence of the uncertainty.

| Source | 0–10% | 10–30% | 30–50% | 50–90% | pp |
|---|---|---|---|---|---|
| Background fluctuation bias | $< 1\%$ | $< 1\%$ | 0% | 0% | 0% |
| Jet fragmentation bias | 0-3% | 0-2% | 0-1% | 0-1% | 0-1% |
| Residual jet energy scale | 2-9% | 2-9% | 2-10% | 2-10% | 1-11% |
| Jet resolution | 1-3% | 1-2% | 1-2% | 1-2% | 1% |
| Tracking efficiency | 6% | 6% | 6% | 6% | 3% |
| Pair-acceptance corrections | 0-1% | 0-1% | 0-1% | 0-1% | 0-1% |
| Background subtraction | 0-3% | 0-3% | 0-3% | 0-3% | 0-3% |
| Total | 7-11% | 7-11% | 7-11% | 7-11% | 4-11% |

Table 3: Systematic uncertainties for the subleading jet shape components, integrated in $\eta$, and $\Delta r$, and shown for pp and centrality binned PbPb collisions. The ranges correspond to the $p_{\mathrm{T}}$ dependence of the uncertainty.

# 7 Results

Figure 1 shows the results for charged particle yields presented differentially in $p_{\mathrm{T}}^{\mathrm{trk}}$, as a function of $|\Delta\eta|$ for the leading jets. The first row shows the charged particle yields without any selection on$x_j$, while other rows show the charged particle yields in different bins of $x_j$ from most unbalanced $0 < x_j < 0.6$ (second row) to most balanced $0.8 < x_j < 1.0$ (fourth row) dijet events. The first panel in each row shows the charged particle yields for the pp collisions while other panels show the charged particle yields for the PbPb collisions in different centrality bins, from most peripheral 50–90% (second panel) to most central 0–10% (fifth panel) collisions. Measurements of the per-jet invariant charged particle yields show an enhancement of these yields in PbPb collisions relative to pp. The enhancement is greatest for central collisions and decreases going to more peripheral collisions. Comparing the different $x_j$ bins for

the leading jet, the enhancement of the total PbPb yield relative to pp yield is seen to slightly increase as the dijet momenta become more balanced. A possible explanation for this is the path length dependence of the energy loss. In balanced dijet events both jets lose significant amount of energy, while in events with unbalanced dijet momenta, the leading jet is produced near the surface of the plasma, thus losing less energy.

Figure 2 shows the results for charged particle yields presented differentially in $p_{\mathrm{T}}^{\mathrm{trk}}$, as a function of $|\Delta\eta|$ for the subleading jets. The results are arranged in the same manner as for leading jets in Fig. 1. As for the leading jets, the measurements of the per-jet invariant charged particle yields for subleading jets show an enhancement in PbPb collisions relative to pp collisions, with the greatest enhancement observed for central collisions. Comparing the different $x_j$ bins for the subleading jet, the enhancement of the total PbPb yield relative to pp yield is seen to slightly increase as the dijet momenta become more balanced. This is opposite to the trend found for the leading jet and may reflect the greater path length through the plasma taken by the subleading jet for more unbalanced dijet events.

The jet radial momentum distributions $\mathrm{P}(\Delta r)$ and jet shapes $\rho(\Delta r)$ are studied by examining the distribution of charged particles in annular rings of width $\delta r = 0.05$ around the jet axis. The transverse momentum profile $\mathrm{P}(\Delta r)$ is the momentum weighted distribution of particles around the jet axis:

$$\mathrm{P}(\Delta r) = \frac{1}{\delta r}\frac{1}{N_{\mathrm{jets}}}\Sigma_{\mathrm{jets}}\Sigma_{\mathrm{tracks}\in(r_a,r_b)}p_{\mathrm{T}}^{\mathrm{trk}} \tag{4}$$

where $\Delta r$ is the angular distance $\sqrt{\Delta\varphi^2+\Delta\eta^2}$ between the charged particle and the jet axis and $r_a$ and $r_b$ define the edges of the ring $\delta r = r_b - r_a$. The jet shape $\rho(\Delta r)$ is the momentum distribution normalized to unity over $\Delta r < 1$, with

$$\rho(\Delta r) = \frac{\mathrm{P}(\Delta r)}{\Sigma_{\mathrm{jets}}\Sigma_{\mathrm{tracks}\in\Delta r<1}\,p_{\mathrm{T}}^{\mathrm{trk}}}\,. \tag{5}$$

Figure 3 shows the jet radial momentum distributions in PbPb and pp collisions. The intervals in track $p_{\mathrm{T}}$ are indicated by the stacked histograms. The first row shows the the jet radial momentum distribution for the leading jets while second row shows the same for subleading jets. The first panel in each row shows the results for the pp collisions while other panels show the results for the PbPb collisions in different centrality bins starting from most peripheral 50–90% (second panel) to most central 0–10% (fifth panel) collisions. For both leading and subleading jets, when going towards more central events, the momentum profile at large $\Delta r$ is enhanced in PbPb collisions over the one in pp collisions. The enhancement is largest for the low $p_{\mathrm{T}}$ charged particles, as expected if the energy lost at high transverse momenta resulting from interactions of partons with quark-gluon plasma reappears in the form of low-$p_{\mathrm{T}}$ particles far away from the jet axis.

Figure 4 shows the PbPb to pp ratio of the jet radial momentum distributions, $\mathrm{P}(\Delta r)_{\mathrm{PbPb}}/\mathrm{P}(\Delta r)_{\mathrm{pp}}$, for different centrality bins. A clear trend can be seen from these ratio plots. The enhancement of the PbPb radial momentum distribution over the pp distribution is the largest for the most central collisions and for larger separations of the charged particles from the jet axis. The enhancement for subleading jets is not as large as for the leading jets because of the widening of the pp reference distribution.

The stacked jet shape results for the leading jets are presented in Fig. 5. The first row shows the

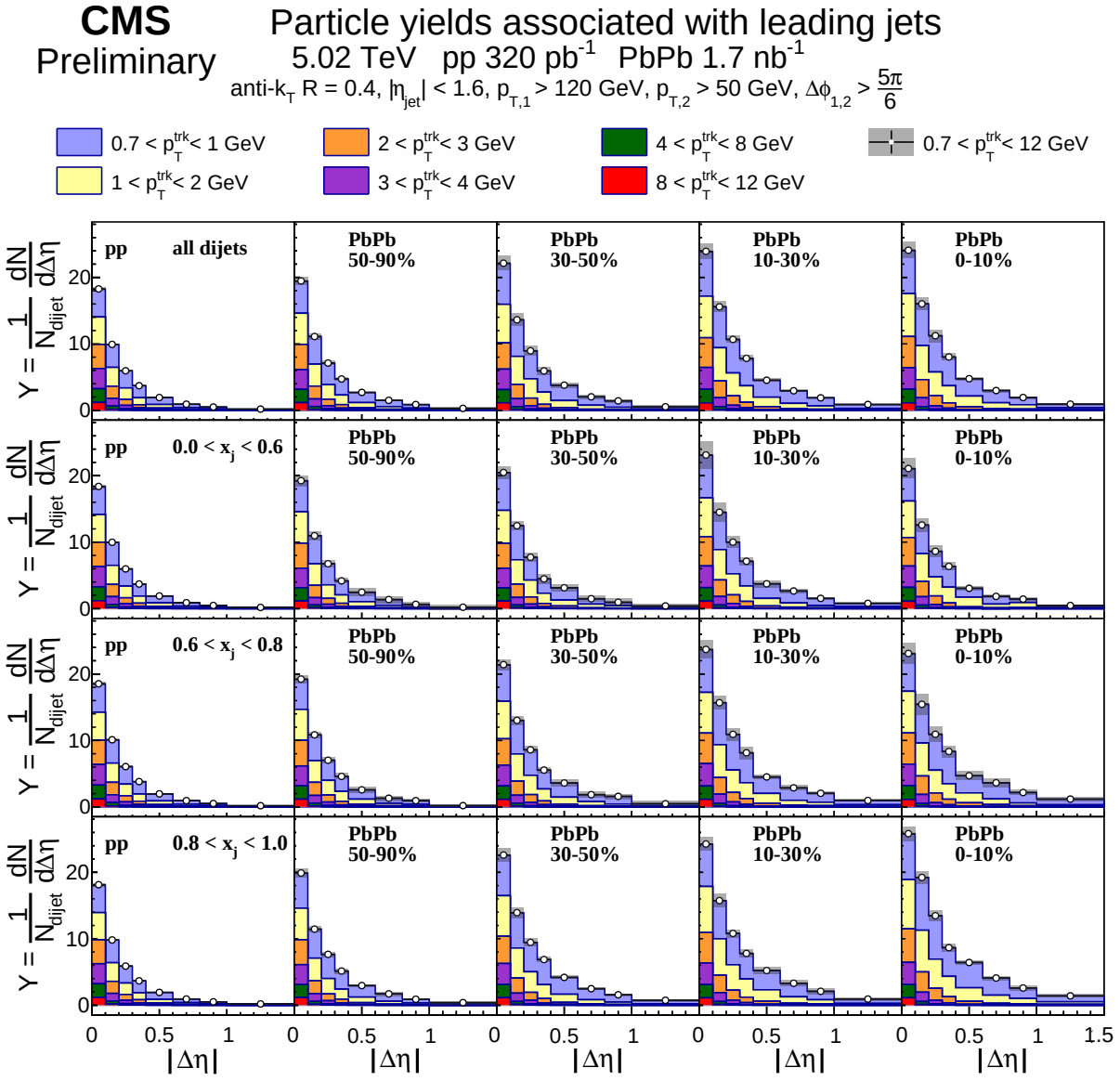


Figure 1: Distributions of charged particle yields correlated to leading jets as a function of $|\Delta\eta|$ for pp (first column) and PbPb collisions in different centrality bins (second to fifth column), shown differentially for all $p_{\mathrm{T}}^{\mathrm{trk}}$ bins. The first row shows the charged particle yields without any selection on $x_j$, while other rows show the charged particle yields in different bins of $x_j$, starting with the most unbalanced $0 < x_j < 0.6$ (second row) to most balanced $0.8 < x_j < 1.0$ (fourth row) dijet events.

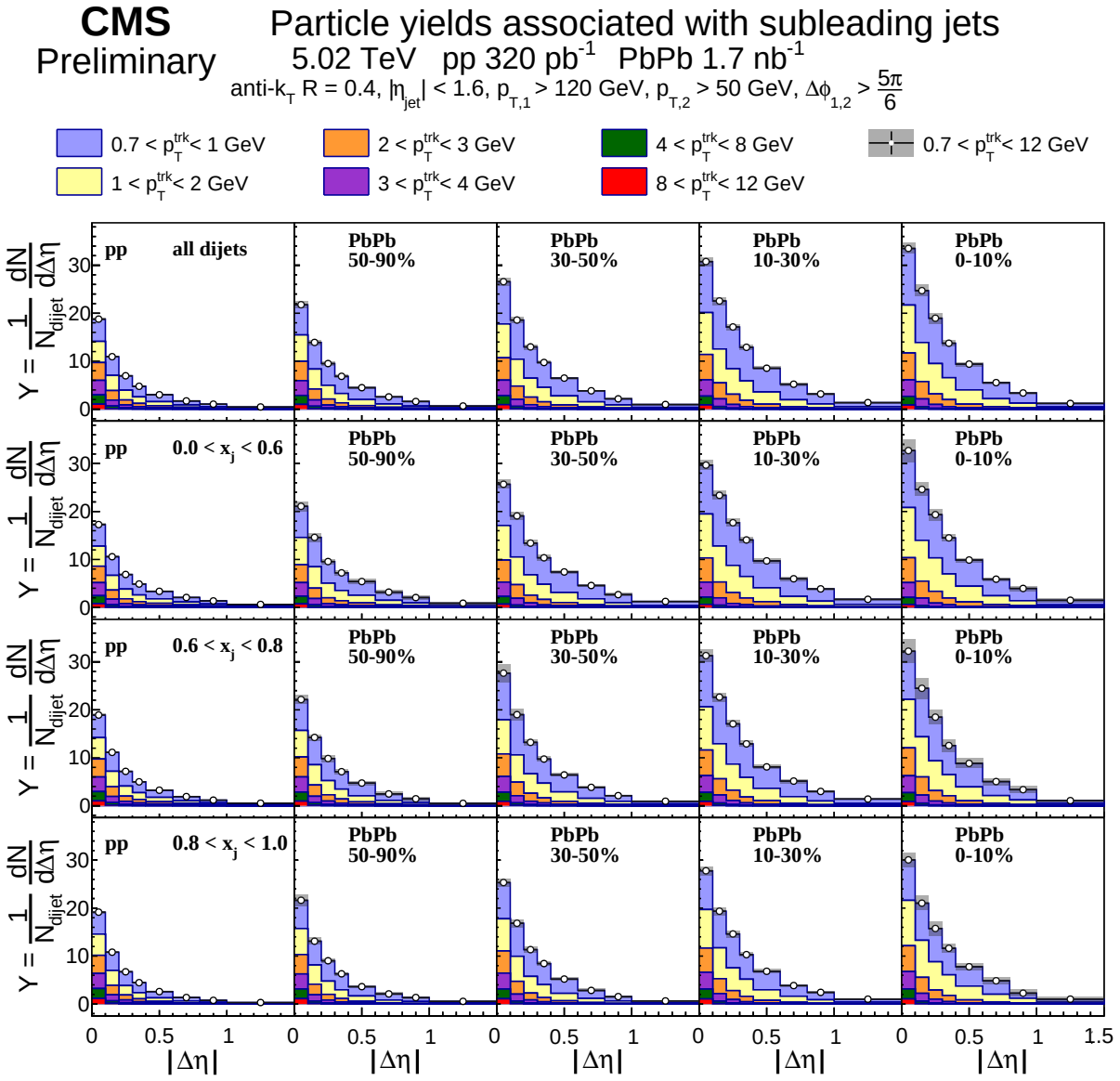


Figure 2: Distributions of charged particle yields correlated to subleading jets as a function of $|\Delta\eta|$ for pp (first column) and PbPb collisions in different centrality bins (second to fifth column), shown differentially for all $p_{\mathrm{T}}^{\mathrm{trk}}$ bins. The first row shows the charged particle yields without any selection on $x_j$, while other rows show the charged particle yields in different bins of $x_j$, starting with the most unbalanced $0 < x_j < 0.6$ (second row) to most balanced $0.8 < x_j < 1.0$ (fourth row) dijet events.

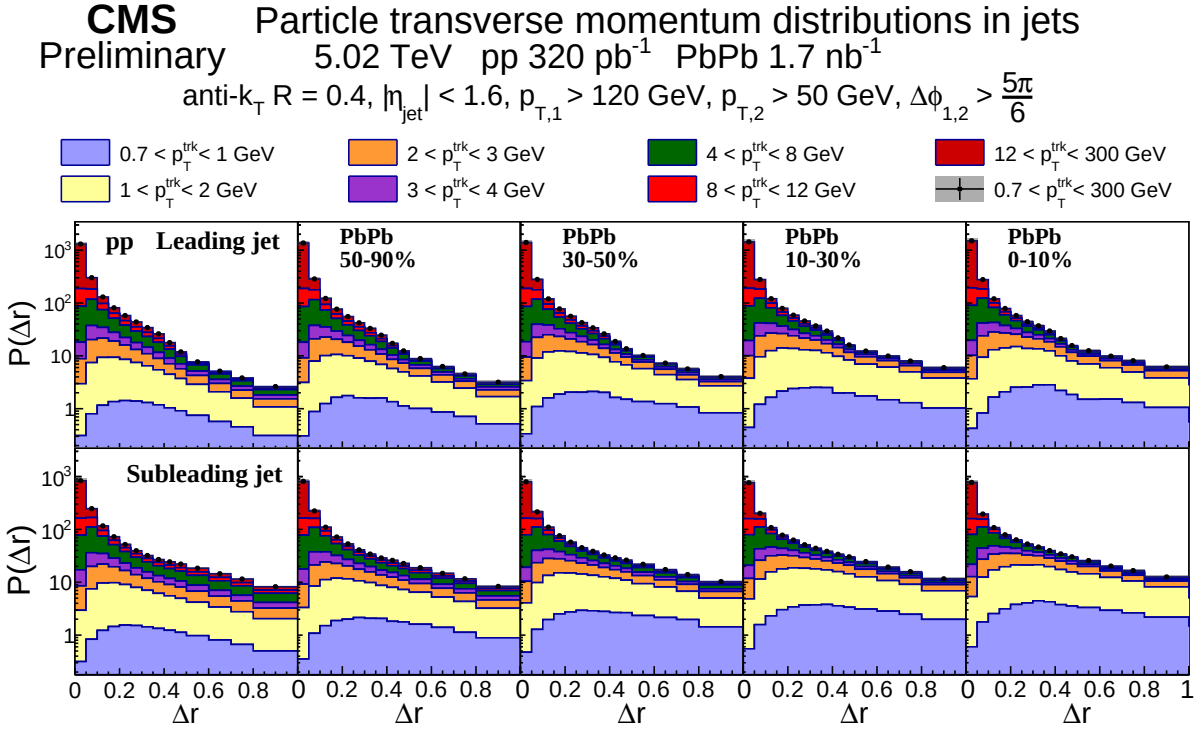


Figure 3: Jet radial momentum profile $\mathrm{P}(\Delta r)$ for pp (first column) and PbPb collisions in different centrality bins (second to fifth column), shown differentially in $p_{\mathrm{T}}^{\mathrm{trk}}$ for leading (top row) and subleading (bottom row) jets.

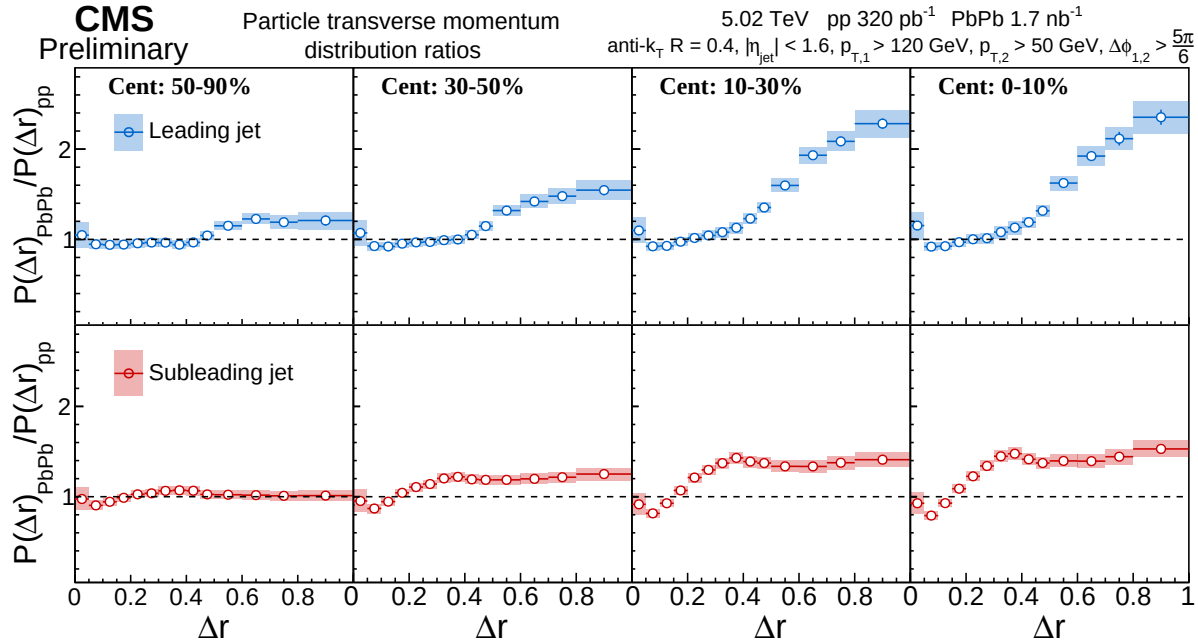


Figure 4: PbPb to pp ratio of the jet radial momentum distributions, $\mathrm{P}(\Delta r)_{\mathrm{PbPb}}/\mathrm{P}(\Delta r)_{\mathrm{pp}}$, for different centrality bins for the leading jets (top row) and subleading jets (bottom row).

jet shape without any selection on $x_j$, while other rows show the jet shape in different $x_j$ bins. The first panel in each row shows the jet shape for the pp collisions while other panels show the jet shape for the PbPb collisions in different centrality bins. When compared to the pp collisions there is an enhancement of low $p_T$ charged particles in PbPb collisions. This enhancement is greater for central events than for peripheral events.

Figure 6 shows the leading jet shape ratio $\rho(\Delta r)_{PbPb}/\rho(\Delta r)_{pp}$, in different centrality and $x_j$ bins. When going towards more central events from the peripheral events, there is an enhancement of PbPb jet shape compared to pp shape. As already seen in the yield plots of Fig. 1, the differences between pp and PbPb results are largest for the most balanced collisions ($0.8 < x_j < 1.0$) and become smaller as the dijet momenta become less balanced.

Figure 7 shows the jet shape results differentially in track $p_T$ for the subleading jets for different selections of centrality and $x_j$. As also found for the leading jet results, an enhancement of low $p_T$ charged particles in PbPb collisions is seen for the subleading jet. There is also a clear peak in the unbalanced pp collision distribution around $\Delta r \sim 0.5$ and a significant contribution to the jet shape is coming from high $p_T$ particles outside of the jet cone. This is still somewhat visible in the peripheral PbPb collisions, but disappears for the central events. In the balanced collisions no peak or enhancement of high $p_T$ particles at large $\Delta r$ are visible. The peak and the enhancement of high $p_T$ particles outside of the jet cone are caused by a third jet contribution in the events. To create an unbalanced dijet configuration in pp collisions, there is likely to be a third jet to conserve momentum. In central heavy ion collisions the momentum can be lost to the medium and no third jet is reconstructed.

The subleading jet shape ratios $\rho(\Delta r)_{PbPb}/\rho(\Delta r)_{pp}$ in different centrality and $x_j$ bins can be found in Fig. 8. When going towards more central events from the peripheral events, there is an enhancement of the PbPb jet shape compared to the pp shape. However, in the most unbalanced ($0.0 < x_j < 0.6$) and moderately balanced ($0.6 < x_j < 0.8$) events the ratio between PbPb and pp jet shapes gets close to one at large $\Delta r$. This can be explained by the disappearance of the third jet in PbPb collisions, as discussed for Fig. 7. If there would be no contribution from particles related to the third jet in the pp jet shape, the enhancement would be the greatest at high $\Delta r$ also in these events, as is currently the case for the most balanced ($0.8 < x_j < 1.0$) events.

The jet shapes in different $x_j$ bins are studied more carefully for leading jets in Fig. 9 and for subleading jets in Fig. 10. These figures show the ratio of jet shapes in momentum balanced and unbalanced samples with the $x_j$ inclusive sample. Taking this ratio cancels the systematic uncertainties related to tracking and jet energy scale. However, uncertainty related to jet energy resolution does not cancel and is included in the systematic uncertainties. For the leading jets, the jet shapes in the unbalanced $0 < x_j < 0.6$ bin are wider than in the $x_j$ inclusive sample and in the balanced $0.8 < x_j < 1.0$ bin the jet shapes are narrower. For the subleading jets in Fig. 10 the behavior is exactly opposite as for the leading jets, the jet shapes in the unbalanced bin are wider and in the balanced bin narrower compared to the $x_j$ inclusive case. This is similar to the $x_j$ dependence seen for the charged particle distributions.

## 8 Summary

CMS has measured charged particle yields in events containing back-to-back leading and subleading jet pairs around the respective jet axes using data from pp and PbPb collisions at $\sqrt{s_{NN}} = 5.02$ TeV collected in 2017 and 2018. Using a momentum weighting, jet shapes are also determined. When comparing the charged particle yields around the jet axes, there is an

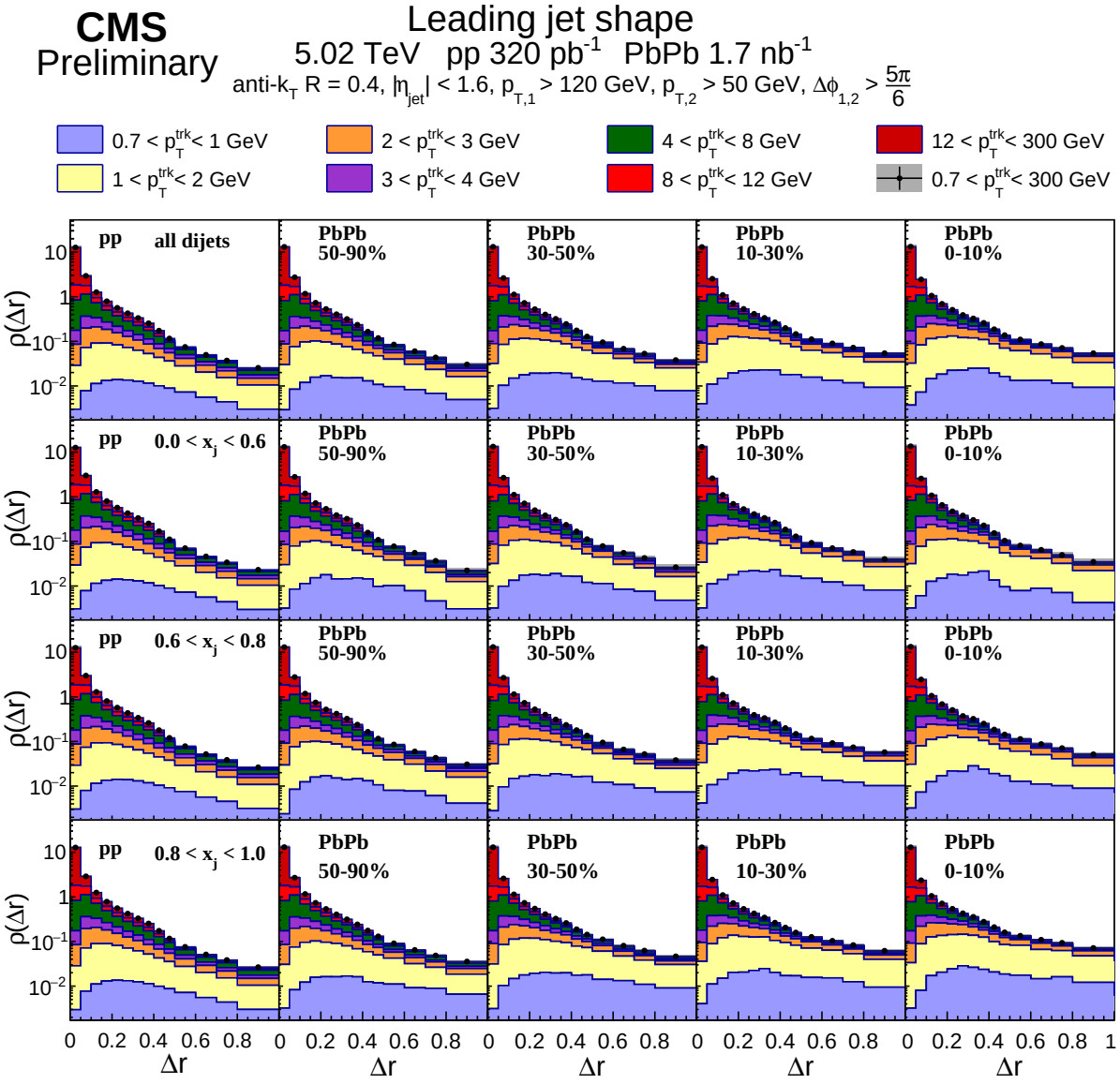


Figure 5: Leading jet shapes $\rho(\Delta r)$ (normalized to unity over $\Delta r < 1$) for pp (first column) and PbPb collisions in different centrality bins (second to fifth columns), shown differentially in $p_{\mathrm{T}}^{\mathrm{trk}}$ for inclusive $x_j$ bin (first row) and in differential bins $0 < x_j < 0.6$ (second row), $0.6 < x_j < 0.8$ (third row), and $0.8 < x_j < 1.0$ (fourth row).

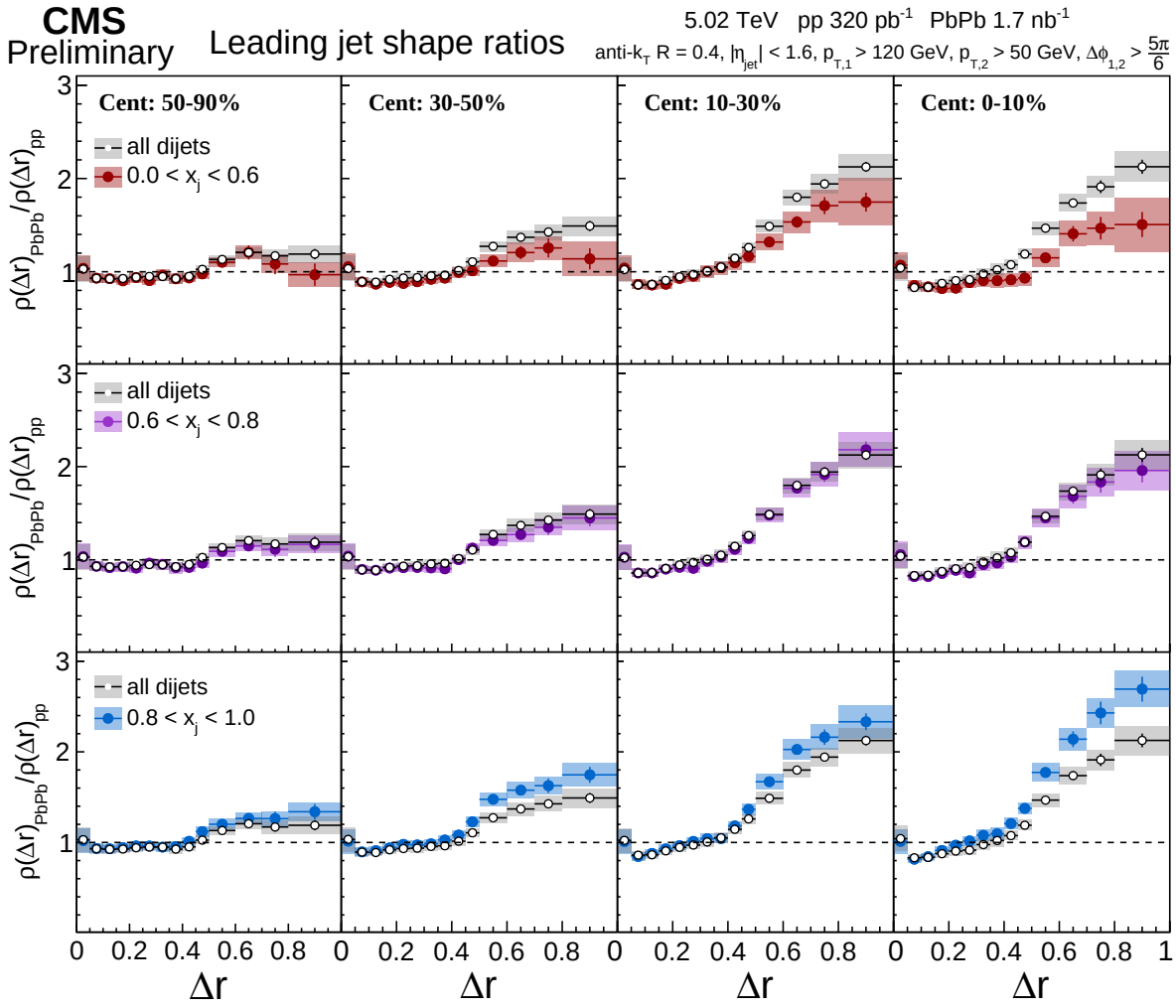


Figure 6: PbPb to pp ratio for leading jet shapes $\rho(\Delta r)_{\mathrm{PbPb}}/\rho(\Delta r)_{\mathrm{pp}}$, in different centrality bins for $0 < x_j < 0.6$ (top row), $0.6 < x_j < 0.8$ (middle row) and $0.8 < x_j < 1.0$ (bottom row) dijet selections. The leading jet shape ratio for all dijets, i.e. without any selection on the dijet momentum balance are also shown in each row for comparison.

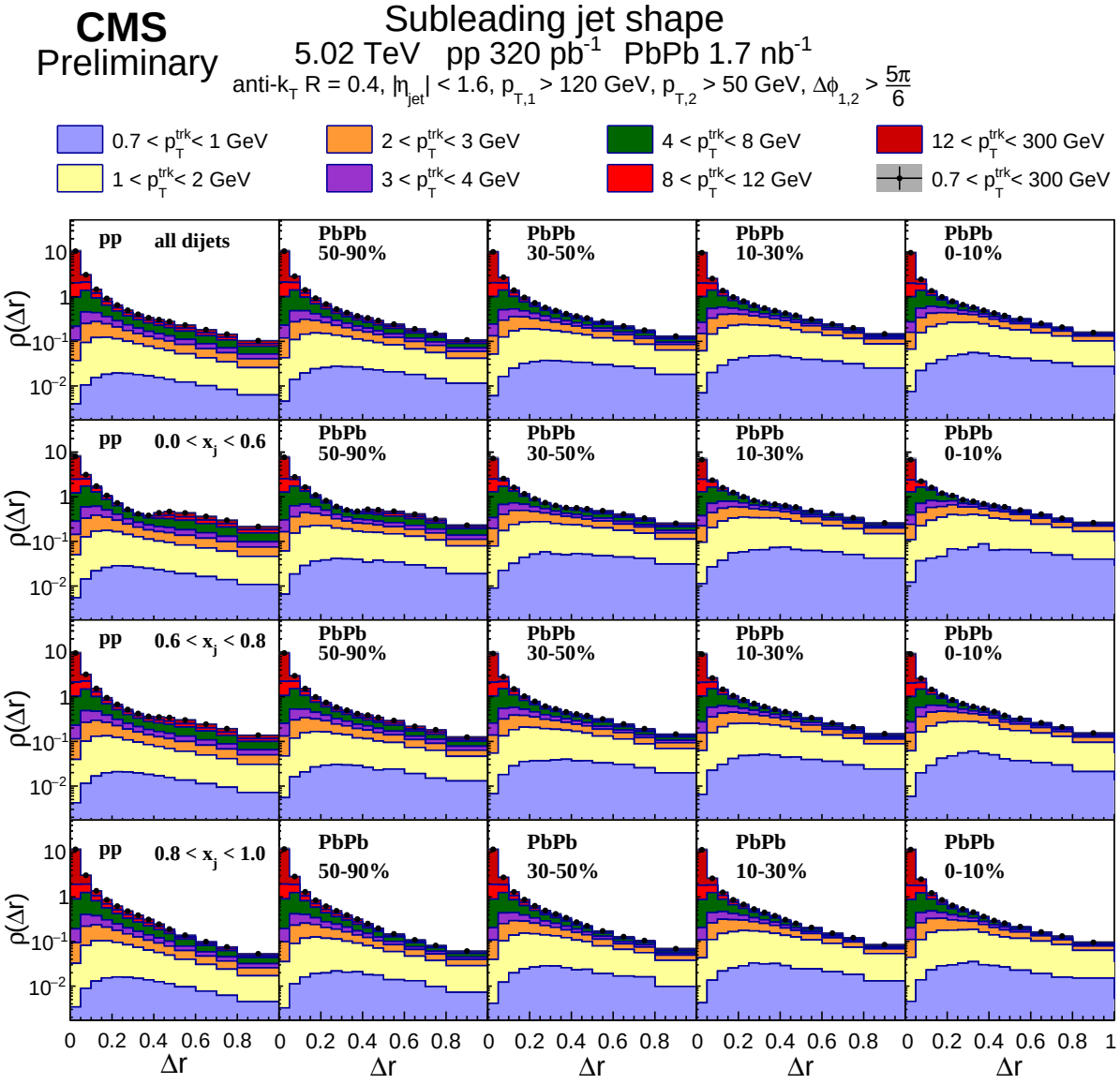


Figure 7: Subleading jet shapes $\rho(\Delta r)$ (normalized to unity over $\Delta r < 1$) for pp (first column) and PbPb collisions in different centrality bins (second to fifth columns), shown differentially in $p_{\mathrm{T}}^{\mathrm{trk}}$ for inclusive $x_j$ bin (first row) and in differential bins $0 < x_j < 0.6$ (second row), $0.6 < x_j < 0.8$ (third row), and $0.8 < x_j < 1.0$ (fourth row).

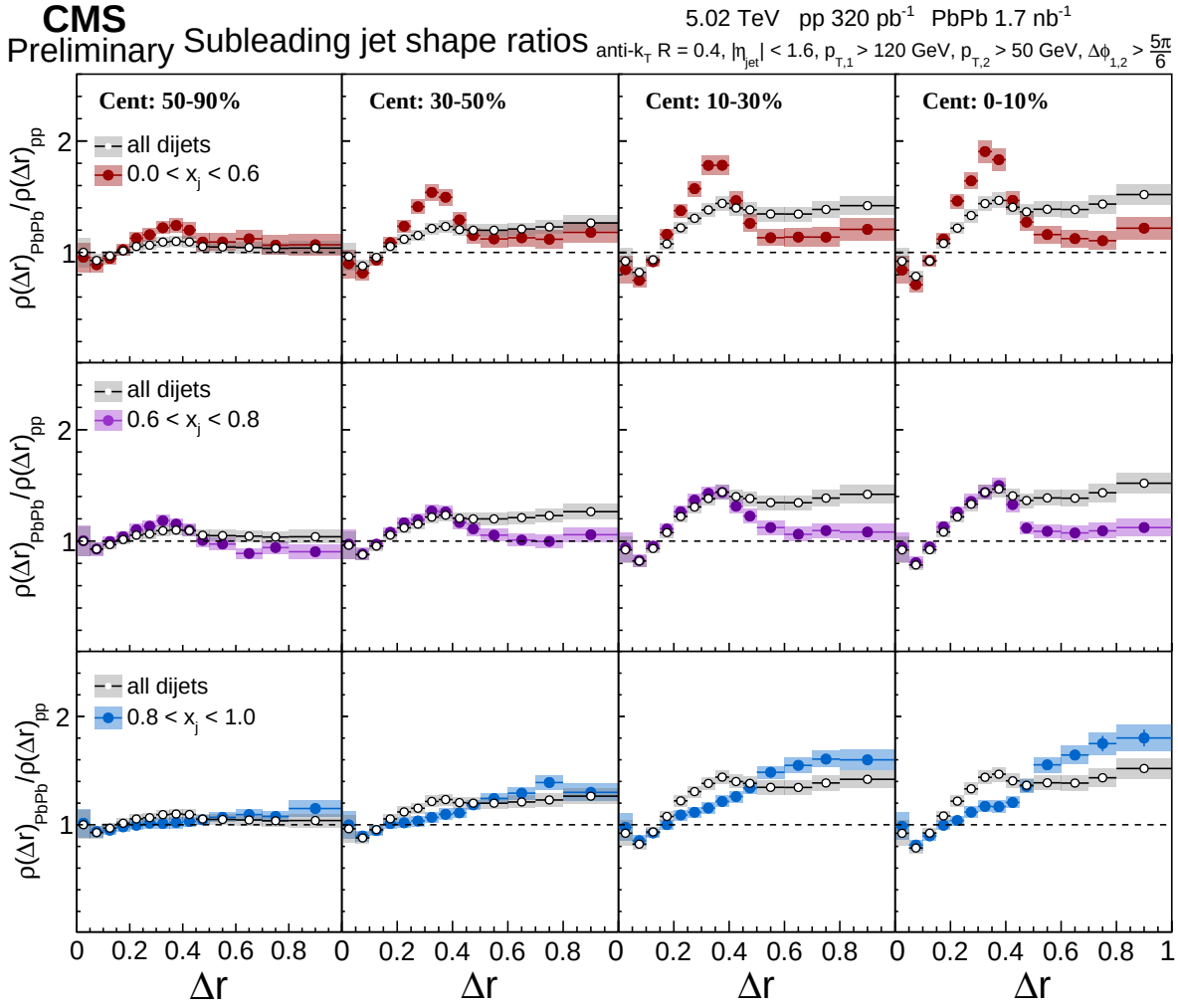


Figure 8: PbPb to pp ratio for subleading jet shapes $\rho(\Delta r)_{\mathrm{PbPb}}/\rho(\Delta r)_{\mathrm{pp}}$, in different centrality bins for $0 < x_j < 0.6$ (top row), $0.6 < x_j < 0.8$ (middle row) and $0.8 < x_j < 1.0$ (bottom row) dijet selections. The subleading jet shape ratio for all dijets, i.e. without any selection on the dijet momentum balance are also shown in each row for comparison.

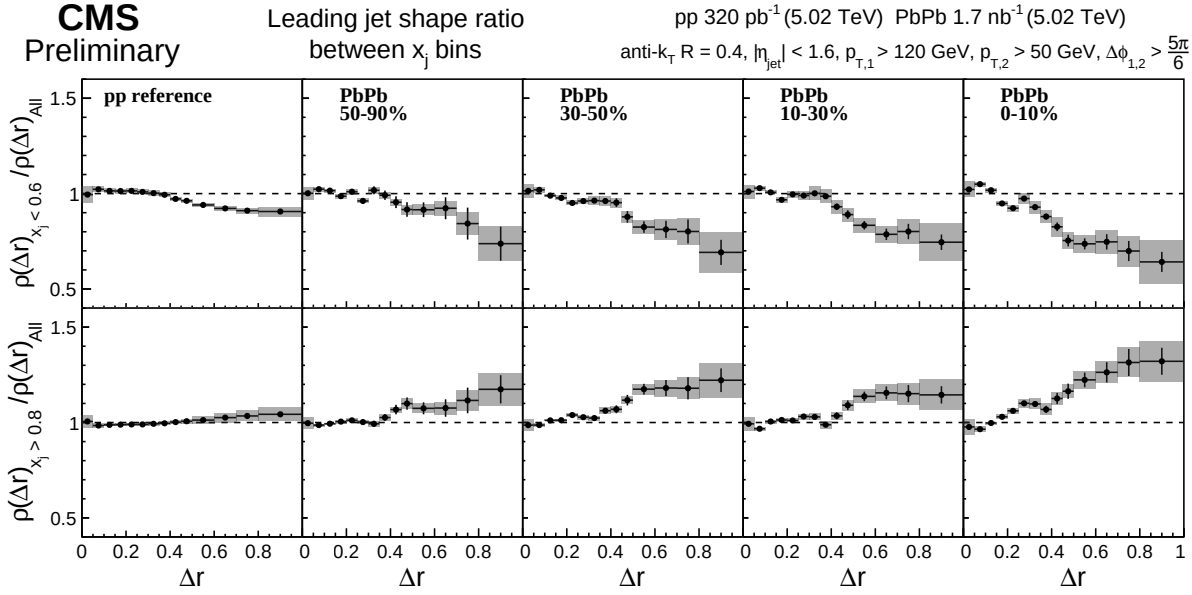


Figure 9: Ratio of momentum unbalanced jet shapes $0.0 < x_j < 0.6$ (top row) and balanced jet shapes $0.8 < x_j < 1.0$ (bottom row) to $x_j$ integrated jet shapes for leading jets in pp collisions and different PbPb centrality bins.

excess of low $p_{\mathrm{T}}$ particles in PbPb collisions with respect to pp collisions. This excess is larger in the subleading side compared to leading side. The excess is also found to have a different $x_j$ dependence for the leading and subleading sides. The leading jets show the strongest modifications effects in balanced events, where the transverse momenta of the two jets are close to each other. However, subleading jets experience the greatest modifications in events with a large jet momentum imbalance between the leading and subleading jets. This indicates that in balanced events both jets lose a comparable amount of energy, while in events with a momentum imbalance the leading jet loses significantly less energy. A possible explanation for the imbalance is that the leading jet is produced near the surface of the plasma while the subleading jet needs to traverse a long distance through the plasma.

For the jet shapes, a redistribution of energy is observed from small angles with respect to the jet axis to larger angles when comparing PbPb collisions to pp events. The difference between the PbPb and pp results is larger for the leading jet compared to the subleading jets, which can be explained by the fact that the subleading jet distribution in pp collisions is significantly wider than that for leading jets. When studying the $x_j$ bins for the subleading jet, there is a peak in the PbPb to pp ratio for unbalanced dijet momentum events that disappears for balanced events. This peak can be attributed to a third jet contribution that is needed in pp events to conserve momentum for events where there is a large dijet momentum imbalance.

When comparing jet shape plots corresponding to different dijet momentum balance conditions, the distributions for leading jets are found to be broader for events with balanced jet momenta compared to those where there is a momentum imbalance. For subleading jets, the situation changes with the events with a significant momentum imbalance found to be broader. These observations are consistent with the previous hypothesis given to interpret the particle yield measurements, namely that the average path length inside the medium for leading jets is larger for momentum balanced events, while for subleading jets it is larger in unbalanced events. These data can be used to constrain models of the production point of the dijet within

the quark-gluon plasma.

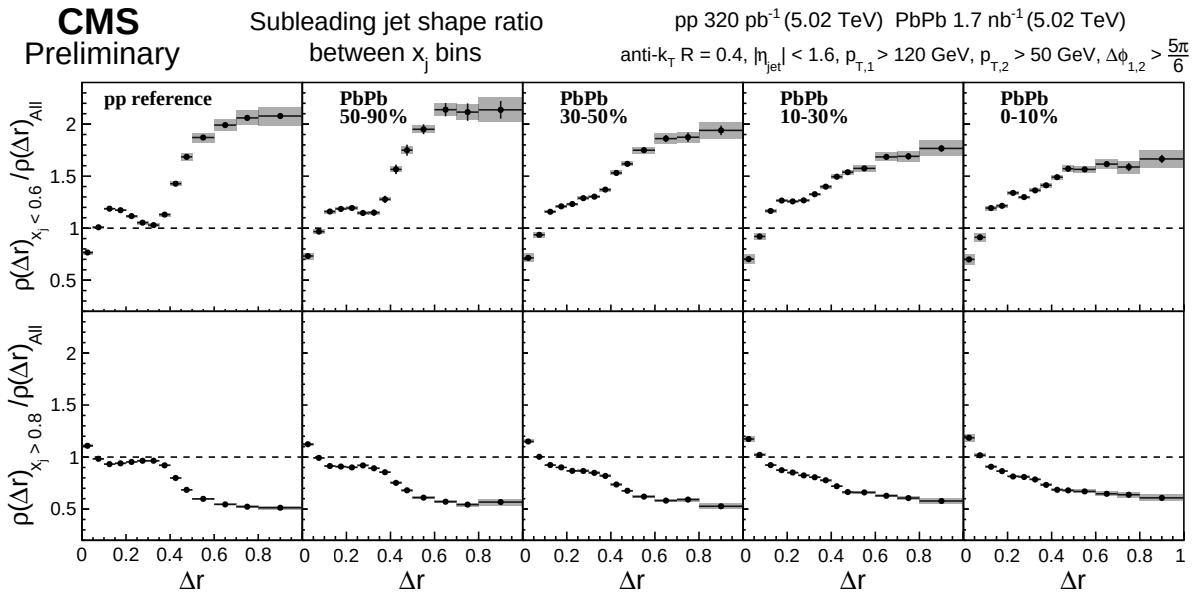


Figure 10: Ratio of momentum unbalanced jet shapes $0.0 < x_j < 0.6$ (top row) and balanced jet shapes $0.8 < x_j < 1.0$ (bottom row) to $x_j$ integrated jet shape for subleading jets in pp collisions and different PbPb centrality bins.

## References


[1] J. D. Bjorken, "Energy loss of energetic partons in qgp: possible extinction of high $p_t$ jets in hadron-hadron collisions", (1982). FERMILAB-PUB-82-059-THY.

[2] STAR Collaboration, "Direct observation of dijets in central Au+Au collisions at $\sqrt{s_{NN}}$ = 200 GeV", *Phys. Rev. Lett.* **97** (2006) 162301, doi:10.1103/PhysRevLett.97.162301, arXiv:nucl-ex/0604018.

[3] PHENIX Collaboration, "Transverse momentum and centrality dependence of dihadron correlations in Au+Au collisions at $\sqrt{s_{NN}}$ = 200 GeV: Jet-quenching and the response of partonic matter", *Phys. Rev. C* **77** (2008) 011901, doi:10.1103/PhysRevC.77.011901, arXiv:0705.3238.

[4] ATLAS Collaboration, "Observation of a Centrality-Dependent Dijet Asymmetry in Lead-Lead Collisions at $\sqrt{s_{NN}} = 2.76$ TeV with the ATLAS Detector at the LHC", *Phys. Rev. Lett.* **105** (2010) 252303, doi:10.1103/PhysRevLett.105.252303, arXiv:1011.6182.

[5] CMS Collaboration, "Observation and studies of jet quenching in PbPb collisions at $\sqrt{s_{NN}}$ = 2.76 TeV", *Phys. Rev. C* **84** (2011) 024906, doi:10.1103/PhysRevC.84.024906, arXiv:1102.1957.

[6] CMS Collaboration, "Jet momentum dependence of jet quenching in PbPb collisions at $\sqrt{s_{NN}} = 2.76$ TeV", *Phys. Lett. B* **712** (2012) 176, doi:10.1016/j.physletb.2012.04.058, arXiv:1202.5022.

[7] ALICE Collaboration, "Measurement of jet suppression in central Pb-Pb collisions at $\sqrt{s_{NN}}$ = 2.76 TeV", *Phys. Lett. B* **746** (2015) 1, doi:10.1016/j.physletb.2015.04.039, arXiv:1502.01689.

[8] CMS Collaboration, "Measurement of jet fragmentation in PbPb and pp collisions at $\sqrt{s_{NN}} = 2.76$ TeV", *Phys. Rev. C* **90** (2014) 024908, doi:10.1103/PhysRevC.90.024908, arXiv:1406.0932.

[9] ATLAS Collaboration, "Measurement of inclusive jet charged-particle fragmentation functions in Pb+Pb collisions at $\sqrt{s_{NN}} = 2.76$ TeV with the ATLAS detector", *Phys. Lett.* **B739** (2014) 320–342, doi:10.1016/j.physletb.2014.10.065, arXiv:1406.2979.

[10] CMS Collaboration, "Modification of jet shapes in PbPb collisions at $\sqrt{s_{NN}} = 2.76$ TeV", *Phys. Lett. B* **730** (2014) 243, doi:10.1016/j.physletb.2014.01.042, arXiv:1310.0878.

[11] CMS Collaboration, "Measurement of transverse momentum relative to dijet systems in PbPb and pp collisions at $\sqrt{s_{NN}} = 2.76$ TeV", *JHEP* **01** (2016) 6, doi:10.1007/JHEP01(2016)006, arXiv:1509.09029.

[12] CMS Collaboration, "Correlations between jets and charged particles in PbPb and pp collisions at $\sqrt{s_{NN}} = 2.76$ TeV", *JHEP* **02** (2016) 156, doi:10.1007/JHEP02(2016)156, arXiv:1601.00079.

[13] CMS Collaboration, "Decomposing transverse momentum balance contributions for quenched jets in PbPb collisions at $\sqrt{s_{NN}} = 2.76$ TeV", *JHEP* **11** (2016) 055, doi:10.1007/JHEP11(2016)055, arXiv:1609.02466.

[14] CMS Collaboration, "Jet properties in PbPb and pp collisions at $\sqrt{s_{\mathrm{NN}}} = 5.02$ TeV", *JHEP* **05** (2018) 006, doi:10.1007/JHEP05(2018)006, arXiv:1803.00042.

[15] L. Apolinario, N. Armesto, and L. Cunqueiro, "An analysis of the influence of background subtraction and quenching on jet observables in heavy-ion collisions", *JHEP* **02** (2013) 022, doi:10.1007/JHEP02(2013)022, arXiv:1211.1161.

[16] A. Ayala, I. Dominguez, J. Jalilian-Marian, and M. E. Tejeda-Yeomans, "Jet asymmetry and momentum imbalance from $2 \to 2$ and $2 \to 3$ partonic processes in relativistic heavy-ion collisions", *Phys. Rev.* **C92** (2015), no. 4, 044902, doi:10.1103/PhysRevC.92.044902, arXiv:1503.06889.

[17] J.-P. Blaizot, Y. Mehtar-Tani, and M. A. C. Torres, "Angular structure of the in-medium QCD cascade", *Phys. Rev. Lett.* **114** (2015), no. 22, 222002, doi:10.1103/PhysRevLett.114.222002, arXiv:1407.0326.

[18] M. A. Escobedo and E. Iancu, "Event-by-event fluctuations in the medium-induced jet evolution", *JHEP* **05** (2016) 008, doi:10.1007/JHEP05(2016)008, arXiv:1601.03629.

[19] J. Casalderrey-Solana et al., "Angular Structure of Jet Quenching Within a Hybrid Strong/Weak Coupling Model", *JHEP* **03** (2017) 135, doi:10.1007/JHEP03(2017)135, arXiv:1609.05842.

[20] Y. Tachibana, N.-B. Chang, and G.-Y. Qin, "Full jet in quark-gluon plasma with hydrodynamic medium response", *Phys. Rev.* **C95** (2017), no. 4, 044909, doi:10.1103/PhysRevC.95.044909, arXiv:1701.07951.

[21] CMS Collaboration, "Jet momentum dependence of jet quenching in PbPb collisions at $\sqrt{s_{NN}} = 2.76$ TeV", *Phys. Lett.* **B712** (2012) 176–197, doi:10.1016/j.physletb.2012.04.058, arXiv:1202.5022.

[22] CMS Collaboration, "Description and performance of track and primary-vertex reconstruction with the CMS tracker", *JINST* **9** (2014), no. 10, P10009, doi:10.1088/1748-0221/9/10/P10009, arXiv:1405.6569.

[23] CMS Collaboration, "The CMS Experiment at the CERN LHC", *JINST* **3** (2008) S08004, doi:10.1088/1748-0221/3/08/S08004.

[24] M. Cacciari, G. P. Salam, and G. Soyez, "The anti-$k_t$ jet clustering algorithm", *JHEP* **04** (2008) 063, doi:10.1088/1126-6708/2008/04/063, arXiv:0802.1189.

[25] O. Kodolova, I. Vardanyan, A. Nikitenko, and A. Oulianov, "The performance of the jet identification and reconstruction in heavy ions collisions with CMS detector", *Eur. Phys. J.* **C50** (2007) 117–123, doi:10.1140/epjc/s10052-007-0223-9.

[26] CMS Collaboration, "Dependence on pseudorapidity and centrality of charged hadron production in PbPb collisions at a nucleon-nucleon centre-of-mass energy of 2.76 TeV", *JHEP* **08** (2011) 141, doi:10.1007/JHEP08(2011)141, arXiv:1107.4800.

[27] T. Sjostrand et al., "An Introduction to PYTHIA 8.2", *Comput. Phys. Commun.* **191** (2015) 159–177, doi:10.1016/j.cpc.2015.01.024, arXiv:1410.3012.

[28] CMS Collaboration, "Extraction and validation of a new set of CMS PYTHIA8 tunes from underlying-event measurements", arXiv:1903.12179.

[29] NNPDF Collaboration, "Parton distributions from high-precision collider data", *Eur. Phys. J. C* **77** (2017), no. 10, 663, doi:10.1140/epjc/s10052-017-5199-5, arXiv:1706.00428.

[30] GEANT4 Collaboration, "GEANT4: A Simulation toolkit", *Nucl. Instrum. Meth.* **A506** (2003) 250–303, doi:10.1016/S0168-9002(03)01368-8.

[31] I. P. Lokhtin et al., "Heavy ion event generator HYDJET++ (HYDrodynamics plus JETs)", *Comput. Phys. Commun.* **180** (2009) 779–799, doi:10.1016/j.cpc.2008.11.015, arXiv:0809.2708.

[32] M. Cacciari, G. P. Salam, and G. Soyez, "FastJet User Manual", *Eur. Phys. J.* **C72** (2012) 1896, doi:10.1140/epjc/s10052-012-1896-2, arXiv:1111.6097.

[33] CMS Collaboration, "Particle-flow reconstruction and global event description with the CMS detector", *JINST* **12** (2017), no. 10, P10003, doi:10.1088/1748-0221/12/10/P10003, arXiv:1706.04965.

[34] D. Bertolini, T. Chan, and J. Thaler, "Jet Observables Without Jet Algorithms", *JHEP* **04** (2014) 013, doi:10.1007/JHEP04(2014)013, arXiv:1310.7584.

[35] A. J. Larkoski, D. Neill, and J. Thaler, "Jet Shapes with the Broadening Axis", *JHEP* **04** (2014) 017, doi:10.1007/JHEP04(2014)017, arXiv:1401.2158.

[36] O. Kodolova, I. Vardanian, A. Nikitenko, and A. Oulianov, "The performance of the jet identification and reconstruction in heavy ions collisions with CMS detector", *Eur. Phys. J. C* **50** (2007) 117, doi:10.1140/epjc/s10052-007-0223-9.

[37] CMS Collaboration, "Measurement of the elliptic anisotropy of charged particles produced in PbPb collisions at $\sqrt{s_{NN}}$=2.76 TeV", *Phys. Rev.* **C87** (2013), no. 1, 014902, doi:10.1103/PhysRevC.87.014902, arXiv:1204.1409.

[38] P. Berta, M. Spousta, D. W. Miller, and R. Leitner, "Particle-level pileup subtraction for jets and jet shapes", *JHEP* **06** (2014) 092, doi:10.1007/JHEP06(2014)092, arXiv:1403.3108.

[39] CMS Collaboration, "Description and performance of track and primary-vertex reconstruction with the CMS tracker", *JINST* **9** (2014) P10009, doi:10.1088/1748-0221/9/10/P10009, arXiv:1405.6569.

[40] CMS Collaboration, "Charged-particle nuclear modification factors in PbPb and pPb collisions at $\sqrt{s_{NN}} = 5.02$ TeV", *JHEP* **04** (2017) 039, doi:10.1007/JHEP04(2017)039, arXiv:1611.01664.

[41] CMS Collaboration, "Measurement of jet fragmentation into charged particles in pp and PbPb collisions at $\sqrt{s_{NN}} = 2.76$ TeV", *JHEP* **10** (2012) 087, doi:10.1007/JHEP10(2012)087, arXiv:1205.5872.

[42] CMS Collaboration, "Jet energy scale and resolution in the CMS experiment in pp collisions at 8 TeV", *JINST* **12** (2017), no. 02, P02014, doi:10.1088/1748-0221/12/02/P02014, arXiv:1607.03663.

# A Dijet momentum balance migration matrices

Jet resolution effects for might cause the $x_j$ of the dijet system to migrate from one bin to another. The magnitude of this effect can be estimated from the simulation. The plots illustrating $x_j$ bin migrations in PYTHIA8 and PYTHIA+HYDJET simulations are presented in Figs. 11 and 12. The plots in Fig. 11 give a probability for the generator level dijet to be in a specific $x_j$ bin, given the $x_j$ bin for the reconstructed dijet while those in Fig. 12 give a probability for the reconstructed dijet to be in a specific $x_j$ bin, given the $x_j$ bin for the generator level dijet. For example, for the PYTHIA8 simulation in the leftmost plot of the top row in Fig. 11, if the reconstructed dijet is in the bin $0 < x_j < 0.6$, the probability that the generator level dijet is also in this bin is 56.5%. It can be seen from these plots that the central heavy collisions are much more smeared than pp collisions in the simulation. In general, the generator level $x_j$ tends to be higher than reconstructed $x_j$, meaning that jet energy smearing causes dijets to be more unbalanced.

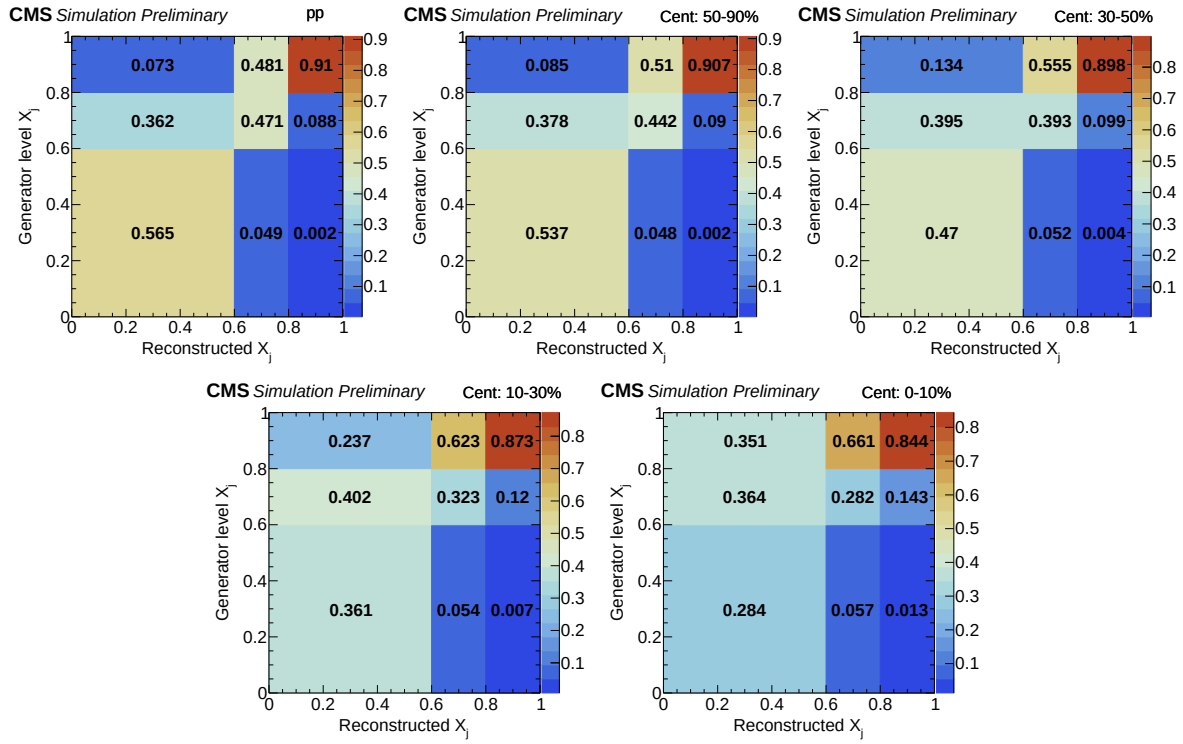


Figure 11: Generator level $x_j$ versus reconstructed $x_j$ in the analysis $x_j$ bins. The plots show the probability to find a generator level $x_j$ for a given reconstructed $x_j$. PYTHIA8 simulation is on the leftmost column in the top row while the most central PYTHIA+HYDJET in on the right of the bottow row.

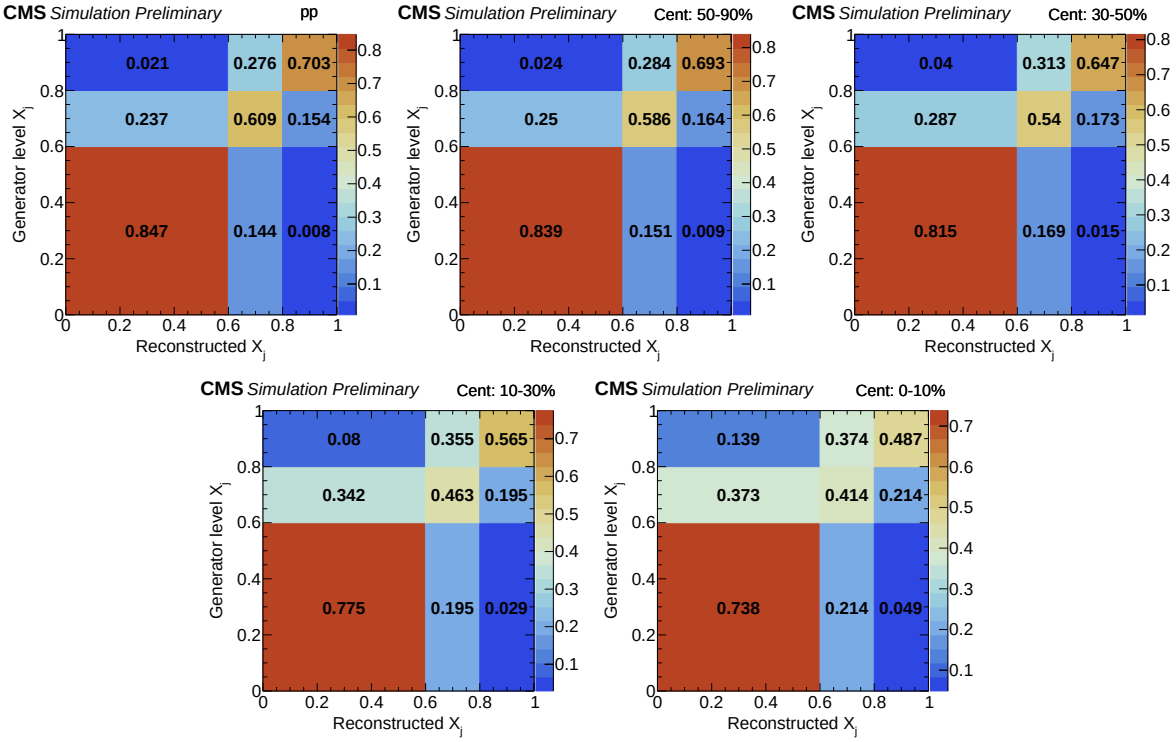


Figure 12: Generator level $x_j$ versus reconstructed $x_j$ in the analysis $x_j$ bins. The plots show the probability to find a reconstructed $x_j$ for a given generator level $x_j$. PYTHIA8 simulation is on the leftmost column in the top row while the most central PYTHIA+HYDJET in on the right of the bottow row.